Case Studies in Construction Materials 21 (2024) e03687

Contents lists available at ScienceDirect

Case Studies in Construction Materials

journal homepage: www.elsevier.com/locate/cscm

Mesoscale simulation method for preplaced aggregate concrete based on physics engine

Chongfeng Xie [a], Xiwang Chen [a,b,*], Jia-Qi Yang [c], Charun Bao [a], Peng Feng [a]

[a] MOE Key Lab of Civil Engineering Safety and Durability, Department of Civil Engineering, Tsinghua University, Beijing, 100084, China
[b] BCEG Advanced Construction Materials Co., Ltd., Beijing, 100015, China
[c] School of Mechanics and Civil Engineering, China University of Mining and Technology (Beijing), Beijing, 100083, China

ARTICLE INFO

Keywords:
Preplaced aggregate concrete
Physics engine
Expansive agent
Mechanical property
Shrinkage behavior

ABSTRACT

Preplaced aggregate concrete (PAC) has up to 60 % aggregate volume content, making mesoscale modelling difficult. A novel mesoscale simulation method based on physics engine was proposed in this study to accurately simulate the coarse aggregate skeleton of PAC. Unlike in conventional mesoscale simulations, point-to-point contacts between aggregates were formed due to virtual gravity in the physics engine. To verify this novel method, mechanical property and shrinkage behavior tests of PAC were conducted under different aggregate gradings and with different expansive agents. For the mechanical property test, the simulation results were compared with the test results in terms of the aggregate stacking state, failure mode, stress–strain curve, and mechanical property parameters. Repeatability and aggregate shape analyses were performed using finite element (FE) model. A similar comparison between the simulation and test results was also performed for the shrinkage behavior. A shrinkage coefficient reflecting the relationship between grout and PAC shrinkage was proposed. This novel mesoscale simulation method based on physics engine is particularly suitable for PAC. However, it is not limited to PAC and can be applied to the simulation of conventional concrete, thus solving the problem of traditional simulation methods that struggle to achieve a high aggregate fraction.

1. Introduction

Preplaced aggregate concrete (PAC), also known as two-stage concrete, is manufactured by preplacing coarse aggregate inside a formwork following the pouring of flowable grout [1]. Either gravity or the pumping method is utilized in the grout pouring process, depending on the component section depth [2]. As shown in Fig. 1, the aggregates form a skeleton through point-to-point contact, and the grout fills the voids in the skeleton. When the concept of PAC was proposed in the 1930s [3], its application was limited to repair and rehabilitation. Subsequently, with maturity, this technique has been utilized in underwater construction, highly reinforced member fabrication, mass concreting, and shielding structures [4].

Compared with conventional concrete, PAC has many advantages. First, the special construction method eliminates the segregation problem that is particularly common in lightweight aggregate concrete [5]. Second, PAC is suitable for all complex shapes, even without the need for vibration. Finally, the coarse aggregate content (approximately 60 % of the total volume) of PAC is higher than that of conventional concrete [6]. This property provides effective protection for nuclear and biological shield concrete [1]. In

* Corresponding author at: BCEG Advanced Construction Materials Co., Ltd., Beijing, 100015, China.
E-mail address: cxw20@mails.tsinghua.edu.cn (X. Chen).

https://doi.org/10.1016/j.cscm.2024.e03687
Received 8 July 2024; Received in revised form 19 August 2024; Accepted 26 August 2024
Available online 2 September 2024

addition, a high coarse aggregate content indicates low dry shrinkage and thermal cracking [7].

For homogeneous materials, an accurate constitutive model can be easily obtained. However, for non-homogeneous materials, the macro behavior is influenced by various mesoscale behaviors in different parts. As a non-homogenous material, PAC, despite having the same constituent materials as conventional concrete, it has different mechanical mechanisms at the mesoscale level. Consequently, an appropriate mesoscale simulation method is essential for PAC.

Commonly, there are five main methods used to simulate the mesoscale behavior of concrete, which are finite element method, discrete element method, lattice element method, lattice discrete particle method and rigid body spring method[8]. Among them, finite element method belongs to continuum method, while others belong to discrete method. Compared to discrete method, the continuum method offers the advantage of explicitly generating the concrete mesostructure, allowing for a more realistic simulation of the aggregate particle size distribution. This makes the continuum method particularly suitable for parameter analysis. Additionally, the continuum method is relatively mature, with various constitutive equations available to simulate the mechanical behavior of raw materials. Discrete element method, the most common discrete approach, can also be used for concrete mesoscale simulation[9–11]. However, it requires more computational resources compared to the continuum method[8]. Furthermore, since discrete element method typically uses spherical particles as the basic unit, it cannot accurately capture the geometry of the mesostructure.

Finite element (FE) method is adopted for the mesoscale simulation of PAC in this work. This method requires the establishment of a geometric model and mesh. Aggregate placement is a key issue in geometric models. Generally, the aggregate placement method can be categorized into three types: random aggregate placement method [12,13], Voronoi graphic method [14], and CT scanning method [15,16]. For the first two methods, it is difficult to reflect the difference between PAC and conventional concrete. In the third method, the simulation is based on fabricated specimens, which means that parameter analysis is difficult to conduct. It can been seen that it is difficult for traditional methods to accurately represent the unique characteristics of PAC. The physics engine method is an ideal solution for PAC aggregate placement because it creates a gravitational field, enabling simulation of aggregate stacking. This method has been attempted in conventional concrete and asphalt concrete modelling, but it has not yet been integrated with finite element (FE) method [15,17].

The main objective of this paper is to propose a novel mesoscale simulation method for PAC that can precisely simulate the coarse aggregate skeleton. To achieve this, physics engine PhysX was used to simulate the coarse aggregate stacking process. The stacking data was then transferred to an FE model. Unlike in conventional mesoscale simulations, point-to-point contacts were formed owing to virtual gravity in physics engine. Mechanical property and shrinkage behavior tests were conducted under different aggregate gradings and with different expansive agents. This novel mesoscale simulation method was used to simulate the test specimens, and the test and simulation results for the mechanical property and shrinkage behaviors were compared.

2. Model methodology

2.1. Mesoscale simulation framework

Fig. 2 shows the flowchart of the novel mesoscale simulation method for PAC. This method comprises two main steps. The first step is to establish a geometric model in which coarse aggregates are preplaced by physics engine. The geometric model contains aggregate information including shape and location. This information is then transferred to the commercial FE software ABAQUS. The second step is to establish an FE model using the background grid mapping method. The element properties, loads, and boundary conditions are also created in this step. The details of these steps are described in the subsequent sections.

2.2. Preplacement of coarse aggregates in a physics engine

To simulate aggregate stacking, an open-source physics engine PhysX, developed by NVIDIA, was used. This physics engine is applicable to scientific simulations involving Newtonian physics based on discrete element method (DEM) [18]. Several attempts have been made at conventional concrete mesoscale simulations using physics engines [15,19]. However, these attempts only used physics engine to compact aggregates, which meant that the random generation of aggregates was still required. In this study, aggregates were generated directly by physics engine.

Before the aggregate generation, a virtual formwork was established as the boundary. The aggregate size was randomly generated according to the aggregate grading. Ten points were randomly selected on a sphere with diameter d to generate convex polyhedral aggregates. These points must be uniformly dispersed on the sphere to avoid malformed aggregates. Therefore, an aggregate point was

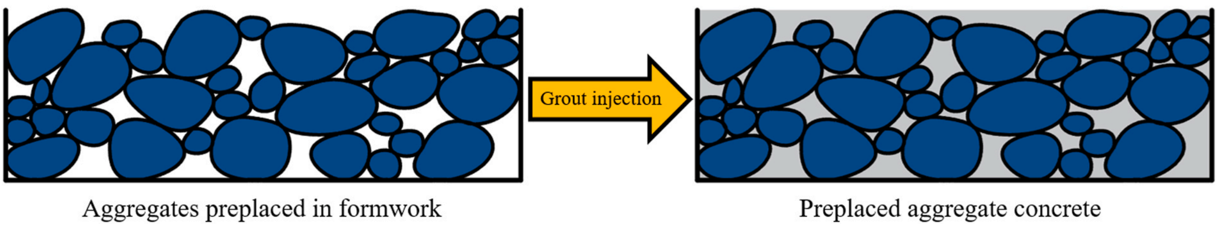

Fig. 1. Casting process of PAC.

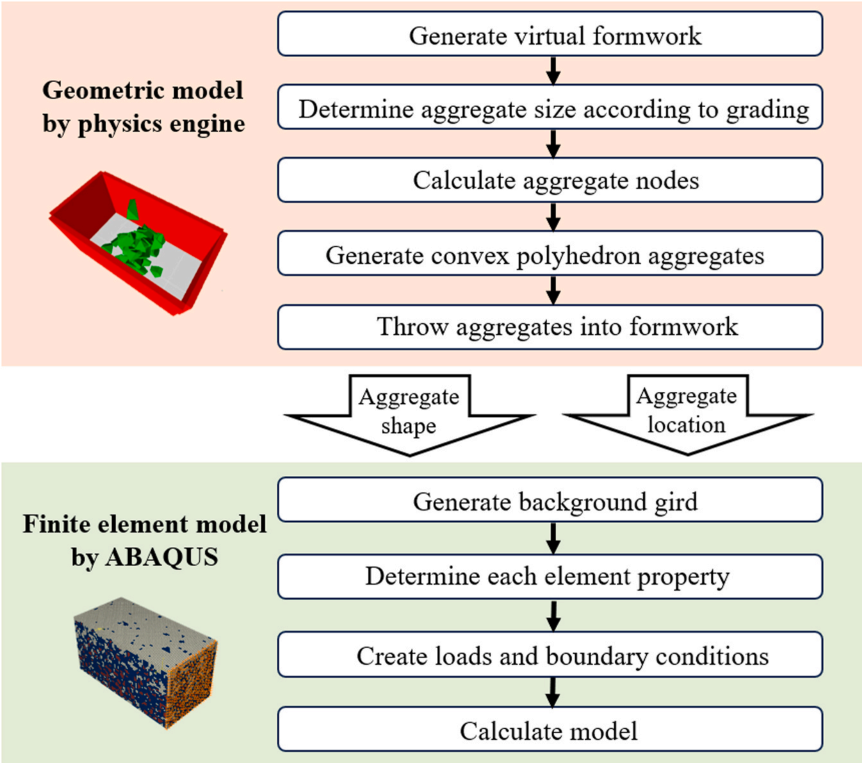

Fig. 2. Flowchart of the novel mesoscale simulation method.

generated at each eighth of the sphere, as shown in Fig. 3. The remaining two aggregate points were randomly generated over the entire sphere. The local coordinates of these points were entered into the physics engine to generate virtual convex polyhedral aggregates. The position, direction, and speed of aggregate throwing were arbitrarily set until they filled the formwork, as shown in Fig. 4. It is important to note that, to ensure that the aggregates fully filled the formwork, some of the aggregates were allowed to overflow from the formwork during the stacking process. Aggregates contained entirely within the formwork were selected based on their positional information. The aggregate information, including aggregate size, global coordinates of aggregate and aggregate nodes, and node numbers of each aggregate face, was output to a text file.

2.3. Discretizing geometric model to FE model

In the discretization process, direct meshing method and background grid mapping method are most commonly utilized [20]. Direct meshing is close to the geometric model information. However, owing to irregular element size and shape, the accuracy of the solution is limited. Background grid mapping method can acquire uniform hexahedral computational grids, which can improve calculation efficiency. However, the similarity between the geometric model and background grid also significantly influences the accuracy of solution. Considering that the aggregate fraction in PAC is high and the minimum aggregate size is small, background grid mapping method was adopted in this study.

Generally, PAC consists of three main phases: aggregate, grout, and interfacial transition zones (ITZ). There are different methods for determining ITZ. The two-phase composite model is the simplest model and ignores the influence of ITZ [5]. To improve accuracy,

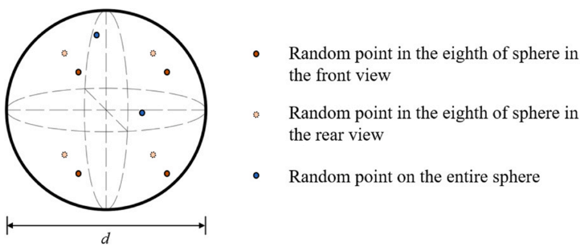

Fig. 3. Random points distribution on the sphere.

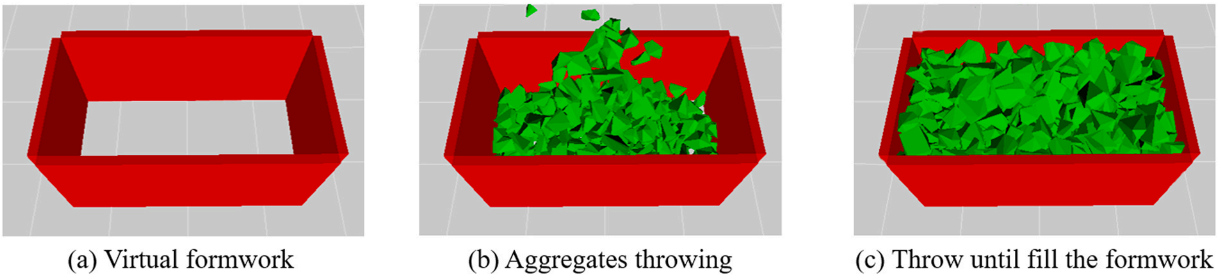

Fig. 4. Aggregate stacking process.

three- and four-phases are also adopted, which is more realistic [21,22]. Compared to conventional concrete, PAC has weaker ITZ, which significantly affects its macro-properties. Therefore, three-phase model including aggregate, grout, and ITZ was adopted in this study.

Background grid mapping procedure is illustrated in Fig. 5. First, background grid was established in ABAQUS using a Python script. Each grid unit was a standard cube. Next, the position of each grid unit node was determined, that is, whether it was in the aggregate, grout, or ITZ. For each grid, the number of nodes in the aggregate was defined as n_a. When $n_a \geq 6$, the grid was defined as an aggregate grid. When $n_a \leq 2$, the grid was defined as a grout grid. When $3 \leq n_a \leq 5$, the grid unit was defined as an ITZ unit. Through background grid mapping, a geometric model with complex shapes was transformed into an easily calculated FE model.

3. Experimental investigation

3.1. Materials and specimens

3.1.1. Raw materials

Coarse aggregate selection is essential in PAC mix design because up to 70 % of the external load is transferred by the aggregate skeleton [23]. Both the shape and grading of aggregate have a significant impact on the grouting, filling, and aggregate content. Bulky rounded or angular aggregates are preferred over flat or elongated aggregates [7]. The void contents of different grading aggregate range from 25 to 50 % [24]. Suitable grading can ensure a production process with lower grout usage. Grout is another important component of PAC. To maintain the strength and flowability of grout, various additives can be added to cement, such as fly ash, limestone powder, silica fume, alkali-activated slag grout, and foamed glass [25–28].

For PAC structures, the maximum coarse aggregate size depends on the dimensions of the structural members. The minimum coarse aggregate size must ensure that the grout flows. Three different coarse aggregate grades were selected for the tests, as listed in Table 1. Fig. 6 demonstrates the coarse aggregate grading curves. The mixing rules are shown in Fig. 7. Grading (A1) is commonly used for conventional concrete. Grading (A2) is composed of grading (A1) and large aggregates. Grading (A3) is a large-sized group without coarse aggregates smaller than 19 mm. The density of aggregates (ρ_a) is 2740 kg/m^3. All the coarse aggregates were washed to keep the surfaces clean, thereby improving the bond between aggregates and grout.

Because the minimum size of the aggregate skeleton was 4.75 mm, sand was not added to the grout. The raw materials included water, cement, additives, and expansive agents. The water–cement (w/c) ratio of the grout was 0.6, which is relatively high. The additive content was 7 % to improve the flowability. Two types of expansive agents were used to compare the effects of different expansive agents on the PAC specimens: calcium sulfoaluminate (CSA) and MgO. The expansion effect of CSA was not evident at a later stage because of the high demand for hydration water [29]. For MgO, the hydration process required less water. Different expansion speeds can be achieved, depending on the hydration reactivity and microstructure [30]. The compressive (f_{gc}) and flexural strengths (f_{gf}) of the grout were obtained from mechanical tests on three 40 × 40 × 160 mm prisms, in accordance with GB/T 29756–2013 [31]. The density (ρ_g) was also measured for each specimen. The average measurement results are listed in Table 2.

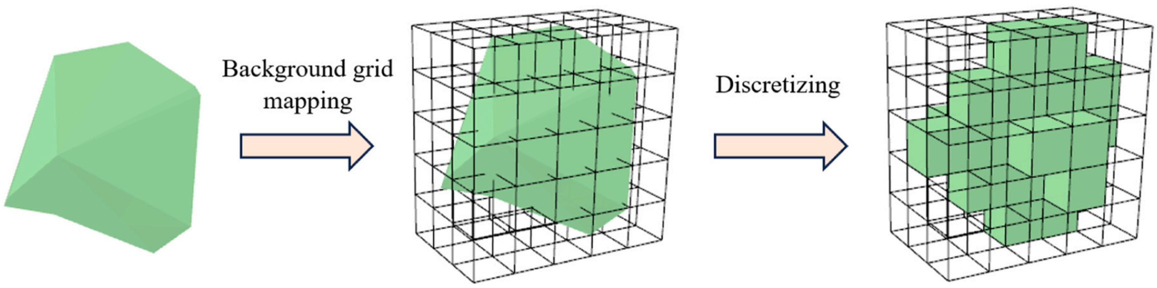

Fig. 5. Background grid mapping procedure.

Table 1
Particle size gradation of coarse aggregates.

Sieve size (mm)	Cumulative percentage passing (%)		
	Grading (A1)	Grading (A2)	Grading (A3)
37.5	–	100	100
31.5	–	90	50
26.5	100	90	50
19	64	57.6	0
16	33	29.7	–
9.5	5	4.5	–
4.75	1	0.9	–

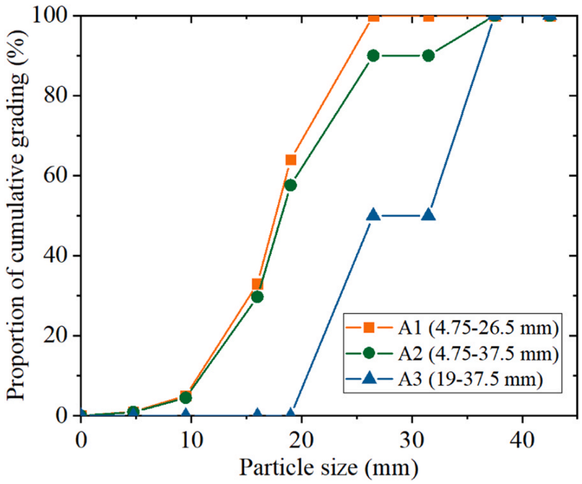

Fig. 6. Cumulative grading curves of coarse aggregates.

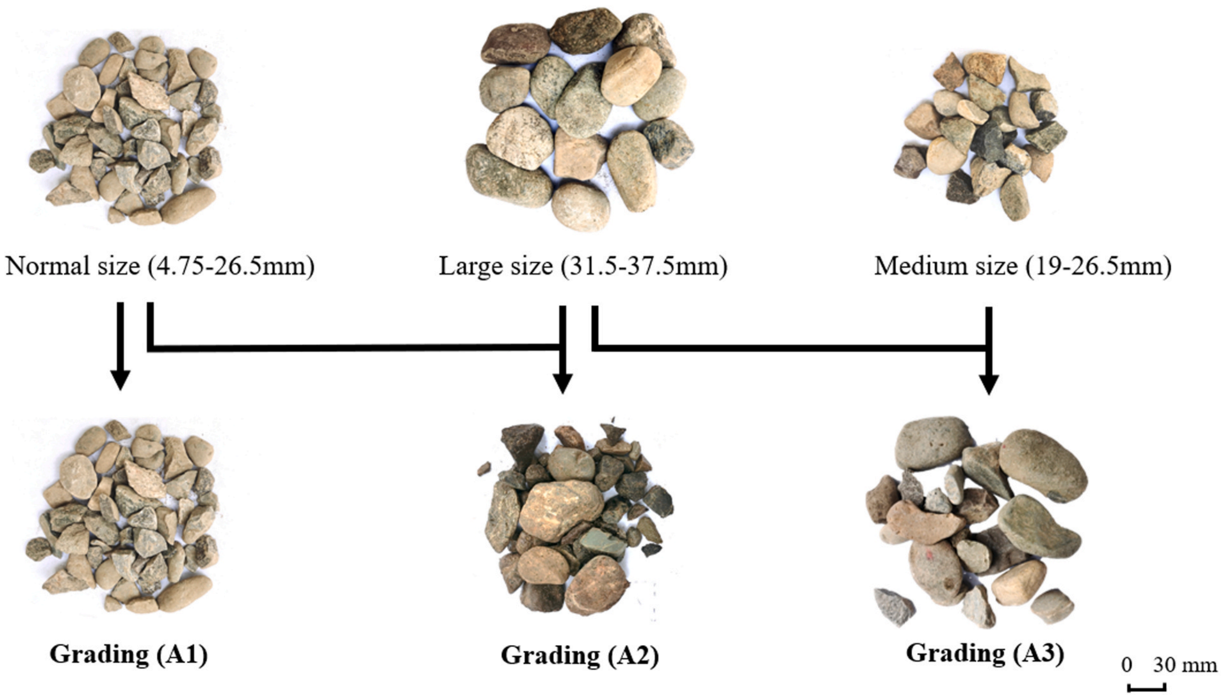

Fig. 7. Mixing rules for coarse aggregates.

3.1.2. Concrete casting

To investigate the compression and shrinkage performance of PAC, two specimen sizes were designed. Three 150 × 150 × 300 mm prismatic specimens were manufactured for the compression test of each PAC type, denoted as Group P. One cylindrical specimen with a diameter of 350 mm and a height of 500 mm was manufactured for the shrinkage test of each PAC type, denoted as Group C. Five types of specimens were manufactured for each group, as listed in Table 3. The influence of aggregate grading and grout type on the A1E0 specimen was studied. The casting process is shown in Fig. 8. To observe the distribution of coarse aggregates in concrete more clearly, the aggregates were dyed red for one of the three specimens in Group P. For Group C, the depth of 800 mm was too deep for a one-time pour. Consequently, the specimen was divided into three parts for separate casting. After all the casting procedures, the specimens were cured at 23 ℃ and a relative humidity of 95 %. The specimens in Group P were removed after 28 d of curing. The specimens of Group C were demolded on the third day, and the shrinkage behavior of concrete under this condition was tested from that day onward. The surface of Group C was smooth after demolding, indicating that full flow of grout was achieved in the aggregate skeleton.

The aggregate fraction is an important parameter that reflects the performance of PAC. For Group C, the coarse aggregate mass m_a was measured. The entire specimen mass M was also measured after curing. The aggregate fraction D_a can be calculated using Eq. (1), and the grout compactness D_g in the aggregate skeleton void can be calculated using Eq. (2).

$$D_a = \frac{m_a/\rho_a}{V} \tag{1}$$

$$D_g = \frac{(M - m_a)/\rho_g}{V - m_a/\rho_a} \tag{2}$$

where V is the volume of the entire specimen based on the standard prism assumption. The calculation results are presented in Table 4. All the specimens had an aggregate fraction level exceeding 50 %. Meanwhile, the selected aggregate grading had no significant impact on the aggregate fraction. Almost all the grout compactness values were above 95 %, reflecting the full flow of the grout.

3.2. Mechanical property test

A concrete compression test was conducted on Group P, in accordance with GB/T 50081–2019 [32]. The effects of the aggregate size and expansive agent type on the compressive performance were investigated. The test setup is illustrated in Fig. 9. Two lateral 100-mm concrete strain gauges and two vertical 150-mm strain gauges were installed on the left and right sides of the specimen. The stress–strain relationship can be obtained by considering the average strain value on both sides as the specimen strain. The loading rate during the test was 0.5 MPa/s. To reduce the impact of non-compact contact between the specimen and machine, the specimen was loaded three times in the initial loading cycle (0.5 MPa to approximately 1/3 of the ultimate load).

3.3. Shrinkage behavior test

The shrinkage properties of Group C were tested. Compared with those of Group P, they had a larger size to reduce the measurement error because concrete dry shrinkage occurs at a very low order of magnitude. The effects of the aggregate size and expansive agent type on shrinkage performance were also investigated. Grout shrinkage tests were performed according to JGJ/T70–2009 [33]. A prismatic specimen with dimensions of 40 × 40 × 160 mm was measured using a digital length comparator for each grout type. The test setup for PAC is shown in Fig. 10. Two dial indicators were placed on both sides using rebars and adaptive screws. The measurement points were located 150 mm from the top and bottom, and the distance between these two measurement points was 500 mm. The average shrinkage value of both sides was considered the specimen shrinkage. Because the specimens required a certain time for hardening, the grout and PAC specimens were demolded three days after casting to initiate the shrinkage measurements. The environment for shrinkage measurement was the same as that for curing. Both the grout and PAC shrinkage tests had a measurement duration of 40 d. Considering that the shrinkage speed was high in the early stages of the test, the shrinkage displacement was measured twice a day for the first 15 d and once a day for the remaining days.

4. Mechanical property simulation discussion

4.1. Aggregate stacking state

The aggregates were randomly placed according to the grading used in the test. The cumulative percentage passing listed in Table 1

Table 2
Properties of grout.

Label	Expansive agent	f_{gc} (MPa)	f_{gf} (MPa)	ρ_g (kg/m^3)
E0	–	35.6	3.05	1754
E1	CSA	38.1	2.51	1757
E2	MgO	38.1	3.73	1779

Table 3
Test specimens for Groups P and C.

Specimen ID	Aggregate grading	Grout type
A1E0	A1	E0
A2E0	A2	E0
A3E0	A3	E0
A1E1	A1	E1
A1E2	A1	E2

Fig. 8. Concrete casting process of Groups P and C.

Table 4
Aggregate fraction and grout compactness of Group P.

ID	D_a (%)	D_g (%)
A1E0	56.6–58.4	92.2–99.5
A2E0	56.9–58.7	97.5–99.8
A3E0	56.8–57.8	98.3–98.7
A1E1	54.5–57.7	97.2–98.1
A1E2	55.8–58.9	96.7–98.9

*Each type consisted of three specimens. The ranges listed in the table indicate the minimum and maximum values for each of the three specimens.

reflects the total aggregate mass for each grading. It is necessary to convert this into an aggregate quantity distribution based on a single aggregate mass. Assuming that the aggregates were standard spheres, the quantity distribution of each grading interval could then be easily acquired. Based on the distribution, aggregates were randomly generated using the physics engine PhysX. To ensure that the aggregates filled the formwork, they were allowed to scatter outside the formwork. Outside aggregates were removed by range checking when outputting the resulting text files. The aggregate fraction was calculated for each grading.

A stacking-state comparison of the simulation and test results is shown in Fig. 11. The dashed blue line represents the aggregate fraction obtained from simulations. The blue-shaded area represents the aggregate fraction range obtained from the test. As shown, the simulation and test results had similar aggregate stacking states. However, compared to the simulation results, the tested aggregates were more rounded. For gradings A1 and A2 with smaller aggregate sizes, the simulated aggregate fraction was slightly higher. For grading A3 with a larger aggregate size, the simulated aggregate fraction was rather low. This may be because the corner of the convex polyhedron was sharper than the actual aggregate shape. Hence, the space between the aggregates was larger. However, for small aggregates, contact overclosure caused more overlap between the aggregates. This canceled out the sharper shape effect and caused the simulated aggregate fraction to be higher than the actual value.

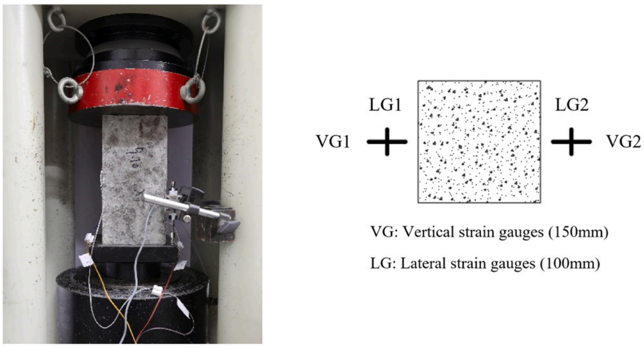

(a) Loading machine (b) Strain gauge placement

Fig. 9. Compression test setup.

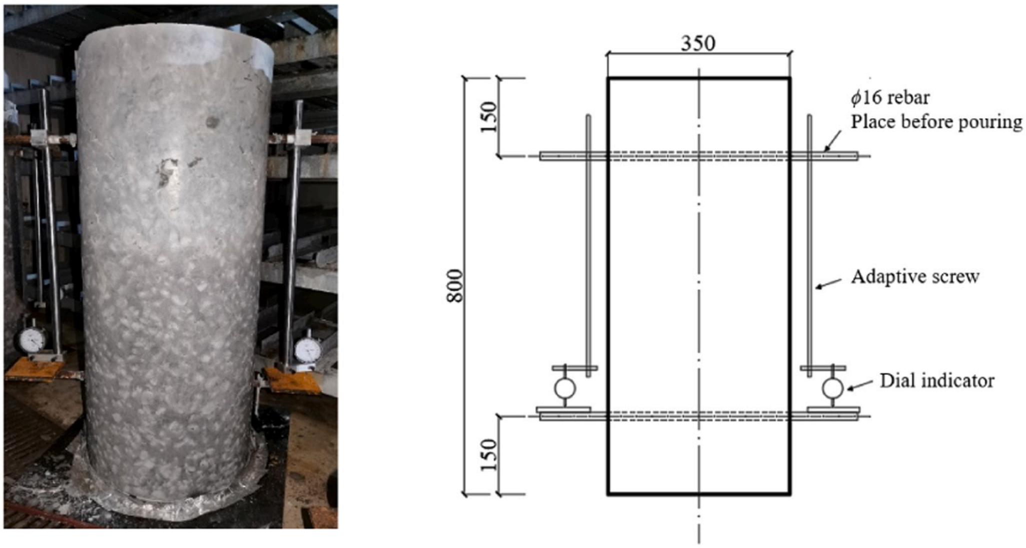

(a) Test setup (b) Details of instrumentation (unit: mm)

Fig. 10. Shrinkage test setup and instrumentation.

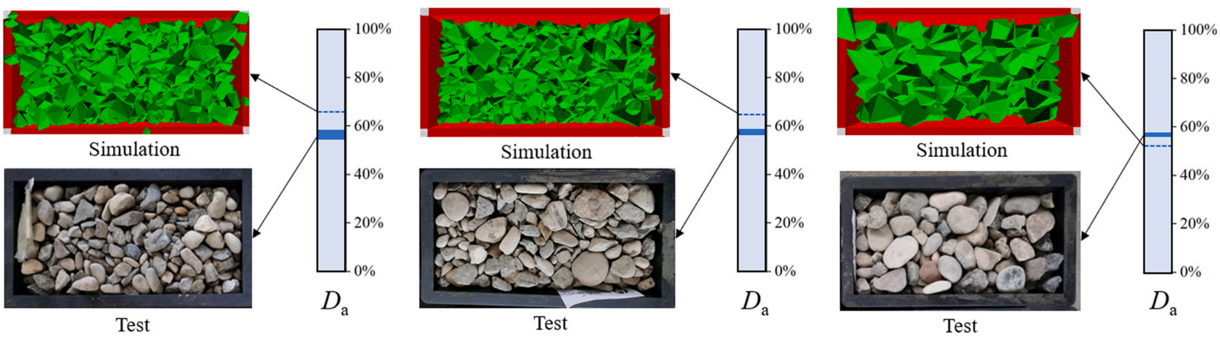

Grading (A1) **Grading (A2)** **Grading (A3)**

Fig. 11. Aggregate stacking comparison.

4.2. Finite element model

An FE model with dimension of 150 × 150 × 300 mm and the same size as the test specimens was established using the commercial FE software ABAQUS. Considering calculation efficiency and accuracy, the size of the background grid was 3.75 mm. Because the strength of PAC is low, damage occurs in the grout and ITZ rather than in the aggregates. As a result, the elastic constitutive model was used for the aggregates, whereas the elastic-plastic model was used for the grout and ITZ. The parameters determined using the constitutive models are listed in Table 5.

The elastic modulus of the aggregates was defined as 50 GPa using the inverse method [34,35]. For the grout, flexural strength was regarded as the tensile strength. The flexural and compressive strengths were consistent with those listed in Table 2. The mechanical behavior of grout is similar to that of concrete [36]. The concrete damage plastic (CDP) model was adopted in the FE model to simulate the grout damage progress [37,38]. The elastic modulus was calculated based on the stress–strain curve. For the ITZ, the constitutive model was more complex. Compared to grout, the ITZ is more porous because of the wall effect, micro-bleeding, nucleation, and precipitation [39]. Therefore, the mechanical properties of the ITZ are poor. Background electron imaging reveals that the thickness of this area can reach 50 μm [39]. In conventional mesoscale simulation, the thickness of the ITZ is generally between 0.05 and 1 mm [40]. However, the aggregate fraction is higher in PAC. Hence, the ITZ content is higher and the shape of the transition zone is more abnormal. To improve the calculation efficiency and broaden its applicability, the ITZ and grout shared the same mesh sizes in the FE model. The ITZ mechanical parameters were obtained by multiplying the grout mechanical parameters by reduction coefficients [41,42]. The construction procedure of PAC results in an inferior ITZ. Therefore, a larger reduction coefficient was required. Using the inverse method, the reduction coefficients for the elastic modulus, compressive strength, and tensile strength were 1/3, 1/9, and 1/9, respectively. The Poisson's ratios of the aggregate, grout, and ITZ were defined as 0.2.

Considering A1E0 specimen as an example, the FE model is shown in Fig. 12. A sparse region of aggregates formed at the top of the specimen owing to the stacking effect, and an aggregate concentration area was formed at the bottom of the specimen. Because of the high aggregate content in the A1E0 specimen, the grout could only form a relatively small volume inside the specimen. In the longitudinal section, breakpoints existed in the vertical direction of the aggregate skeleton. This implies that there is no integral aggregate skeleton at the 2D level. This phenomenon verifies the necessity of a 3D model. All the nodes on one side were coupled to the reference point, and the axial load acted on the reference point. Meanwhile, only the longitudinal freedom was preserved for the reference point. For nodes on the other side, the longitudinal freedom was constrained. On this constrained surface, the bottom nodes were constrained in the vertical direction, and the back nodes were constrained in the transverse direction. The grout, aggregate, and ITZ were set as C3D8R elements to avoid the shear self-locking effect and improve computational stability.

4.3. Comparison of test and simulation

4.3.1. Failure mode

The failure modes of the test specimens and FE model are shown in Fig. 13. The top, side, and bottom views correspond to the positions of the specimens during casting. For ease of observation, obvious cracks on the specimen are indicated by yellow lines. For each test group, only one of the three specimens is presented, for which the aggregates were dyed. In the FE model, the distribution of equivalent plastic strain is illustrated. Owing to grout shrinkage during specimen curing, the top face of the specimen was uneven. This phenomenon was more obvious in the groups without an expansive agent, namely, A1E0, A2E0, and A3E0. Failure predominantly occurred in the grout and ITZ, validating the assumption that the aggregates were not damaged. The cracks mostly developed longitudinally and attached to the aggregates. Crack propagation was concentrated near the edges and corners, leading to grout detachment. Some specimens exhibited more severe damage at the top face than at the bottom, or vice versa. However, this phenomenon was random. Within some groups, these two opposing phenomena were observed for all three specimens. The results of the FE model agreed well with the test results. Areas near the edges often exhibited higher plastic strains, and noticeable local damage occurred at some corners and edges. However, owing to the limitations of the FE method, simulating the later stage of the concrete spalling process was challenging.

With respect to the effect of aggregate grading, a smaller aggregate size resulted in denser cracks. The damage patterns were essentially the same, with local crack propagation leading to grout spalling in all groups. Regarding the effect of the grout type, differences were only reflected in the top faces of the specimens. The A1E0, A1E1, and A1E2 FE models used the same aggregate data

Table 5
Constitutive model parameters.

Properties	Aggregate	E0	E1	E2	E0 ITZ	E1 ITZ	E2 ITZ
Elastic modulus (GPa)	50[a]	30.9[b]	30.8[b]	30.8[b]	10.3[a]	10.3[a]	10.3[a]
Compressive strength (MPa)	–	35.6[b]	38.1[b]	38.1[b]	4.0[a]	4.2[a]	4.2[a]
Tensile strength (MPa)	–	3.05[b]	2.51[b]	3.73[b]	0.34[a]	0.28[a]	0.41[a]
Dilation angle	–	38°[c]					
Eccentricity	–	0.1[c]					
fb0/fc0	–	1.12[c]					
K	–	0.667[c]					
Viscosity parameter	–	0[c]					

Note: Data "a" were acquired through inverse method; Data "b" were acquired through mechanical tests; Data "c" referred to the literature [37,38].

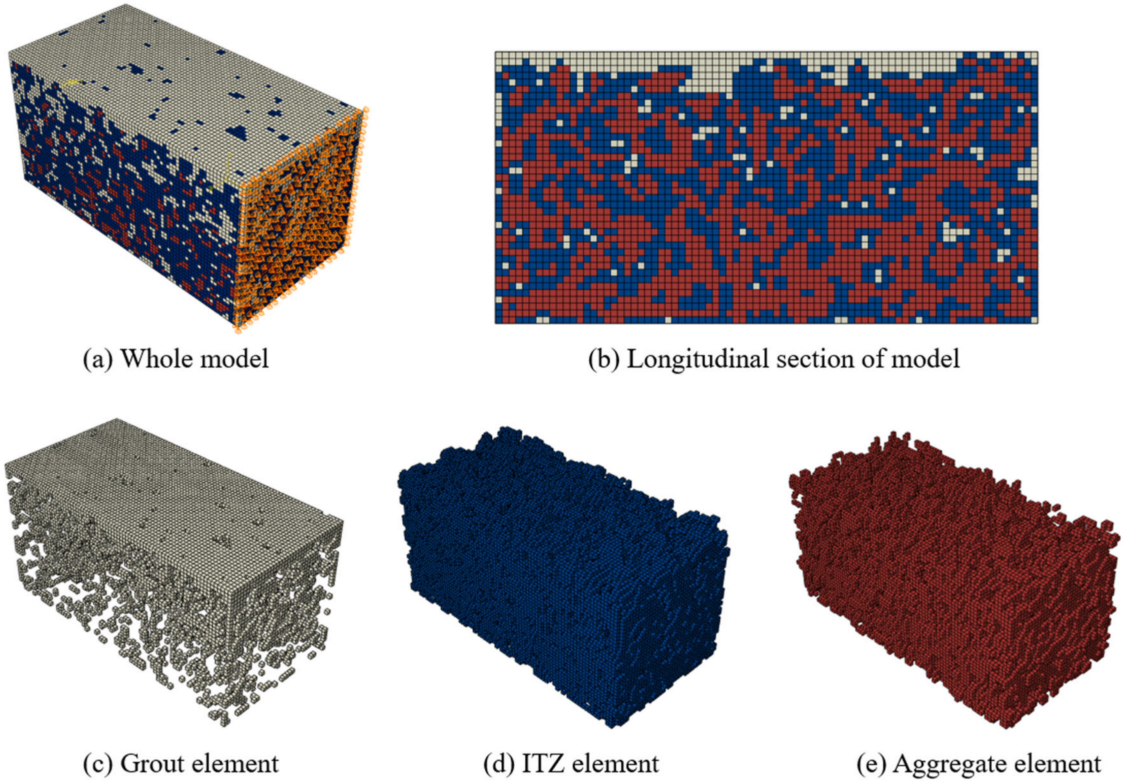

Fig. 12. Mechanical FE model of the A1E0 specimen.

and thus exhibited similar simulated damage patterns. However, owing to the different stress–strain relationships of the different grouts, the ultimate states at the end of the calculation were different.

4.3.2. Stress–strain curve

Fig. 14 shows a stress–strain curve comparison between the test and FE model. The endpoint of the curve corresponds to the moment of strain gauge failure. Therefore, the ultimate strength of the specimen may not be equal to the peak value. In the same group, the elastic modulus at the initial stage were almost identical. However, the stress–strain curves softened as cracks developed. The ultimate strain may also differ significantly within the same group. Taking the A3E0 group as an example, the ultimate strain of A3E0–1 was approximately 140 % higher than that of the other two specimens. This may be due to the poor mechanical properties of the ITZ in PAC. ITZ destruction occurred in the late loading stage, which led to local failure of the specimens. Nonetheless, the overall aggregate skeleton could withstand the load. The stress in the members continued to increase while the stiffness gradually decreased. Owing to the differences in the contact between the aggregates, some specimens quickly suffered global damage, whereas others were still able to sustain the load within a certain deformation. Residual deformation of concrete occurred during the initial loading cycle stage. This phenomenon was particularly evident in the group using grout without an expansive agent. This could be attributed to the plastic deformation of the porous ITZ during the loading cycle. With the addition of an expansive agent, the mechanical properties of the ITZ were improved and plastic deformation was reduced.

For the FE model, the failure process was non-uniform. The model was analyzed using implicit static calculation method, and the localized failure of the grout led to the premature termination of the simulation. Consequently, the stress-strain curve lacked a descending section. The simulation results in the elastic stage were consistent with the test results. However, there were some differences in the plastic stage. This is because it was difficult for the ITZ element to simulate the slip between the aggregates and the grout. Therefore, it exhibited limited ductility. It is noteworthy that the FE calculation results for A1E1 and A1E2 were significantly different from the test results. An increase in the grout strength led to more local brittle failure, which led to a decrease in the ultimate deformation of the model. However, the use of an expansive agent improved the performance of the ITZ, and the ductility of the specimen increased during test. For PAC specimens with an added expansive agent, more test results are required to modify the ITZ property parameters.

*For test specimen A1E0–1, the ultimate stress was incorrectly estimated. During the initial loading cycle, the specimens exhibited wide stress ranges.

4.3.3. Mechanical property parameters

To more clearly compare the differences between the FE and test results, the mechanical property parameters of the test and FE

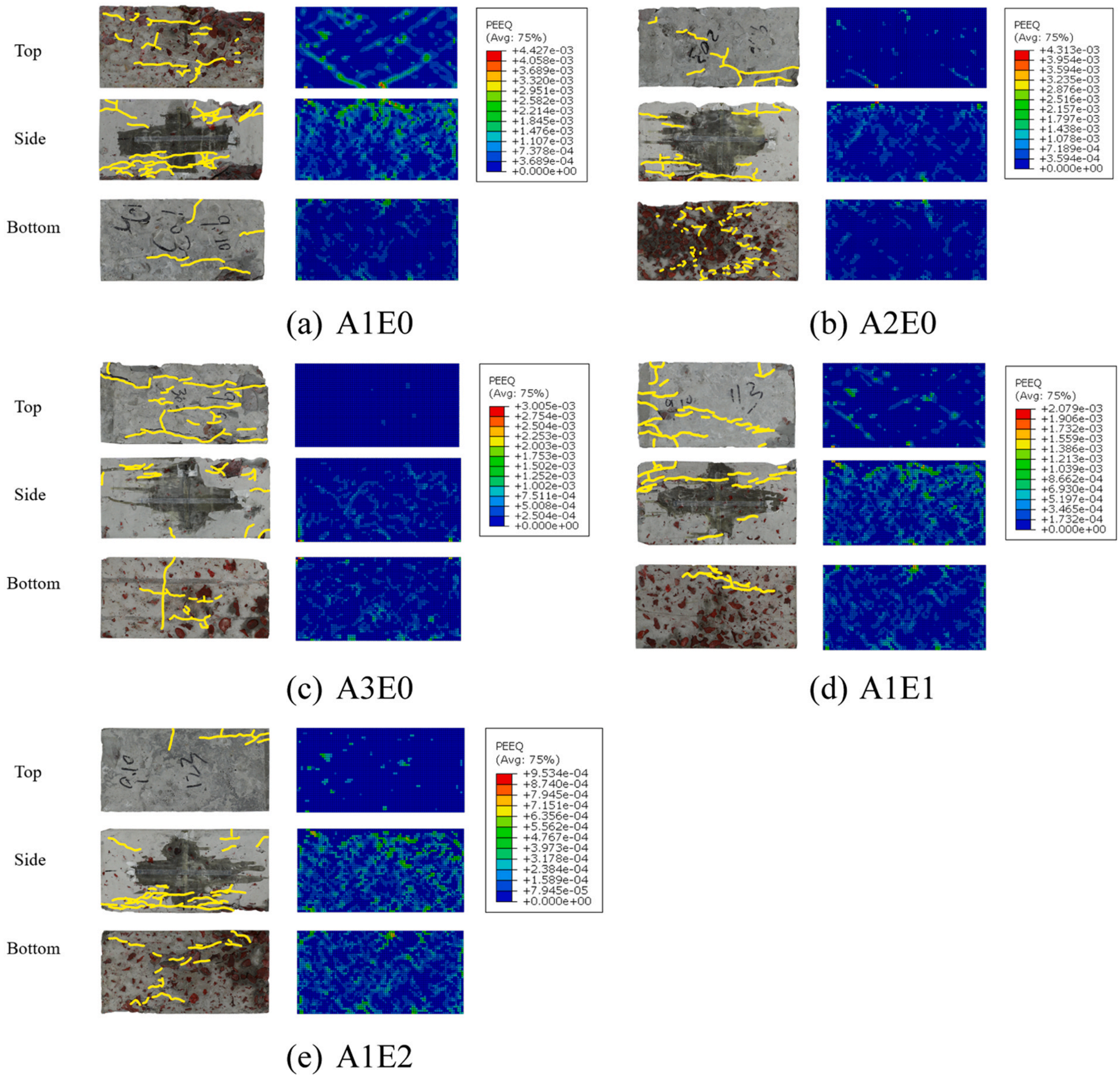

Fig. 13. Comparison of failure modes between the test and FE model.

results are shown in Fig. 15. The standard deviation and mean values were calculated for the test results. The elastic modulus was obtained from the initial stage of the strain–stress curve. Poisson's ratio was calculated from the vertical and lateral strain values at the elastic stage. For the FE model, the vertical strain was obtained from the overall displacement, whereas the lateral strain was obtained from the displacement of the nodes in the middle section at a distance of 100 mm. The test specimen strengths were calculated using the peak force of the loading machine. The peak value of the stress–strain curve was regarded as the strength of the FE model.

When no expansive agent was added to the grout, the variation tendencies of the elastic modulus and Poisson's ratio of the FE model were nearly consistent with the test results. The elastic modulus of the FE model was low in groups with small aggregate sizes. Because the actual ITZ thickness is smaller than the grid size, more aggregate areas are identified as the ITZ, causing a lower elastic modulus. This deviation may be considered acceptable for small aggregate size ranges. The FE results exhibited a relatively high Poisson's ratio compared with the test results. This difference may be because even in the elastic stage, part of the ITZ suffers failure. The failure mode of the CDP model differed from the actual failure mode, leading to a greater volume expansion. A notable discrepancy existed in the simulation of the specimen strength. This discrepancy originated from the correlation between the specimen strength and ductility. Local damage to the aggregate skeleton, which contributes to ductility, is a challenge in FE simulations. This influence was more remarkable in the groups with larger aggregate sizes, which stress–strain curve behaved bilinearly. In practical use, the FE results can be applied as a conservative design value considering the significant discretization of PAC.

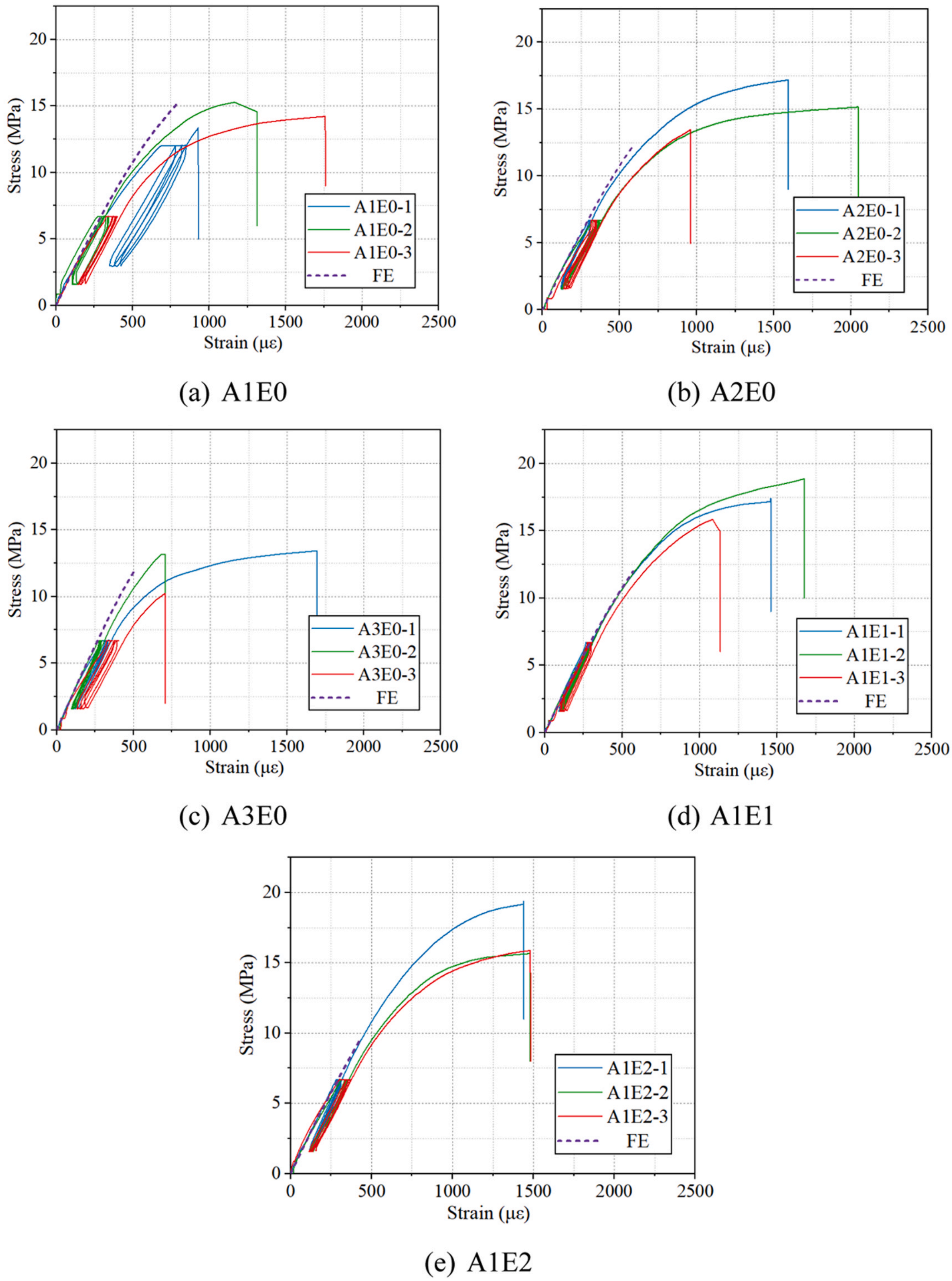

Fig. 14. Stress–strain curve for the test and FE model.

After adding expansive agent to the grout, the mechanical properties of the ITZ were improved. Consequently, the elastic modulus and strength also improved. However, the improved mechanical properties of the ITZ were not properly reflected in the FE model, leading to overestimated simulation results. To reduce this overestimation, additional specimens must be tested using an expansive agent to acquire accurate ITZ mechanical property parameters.

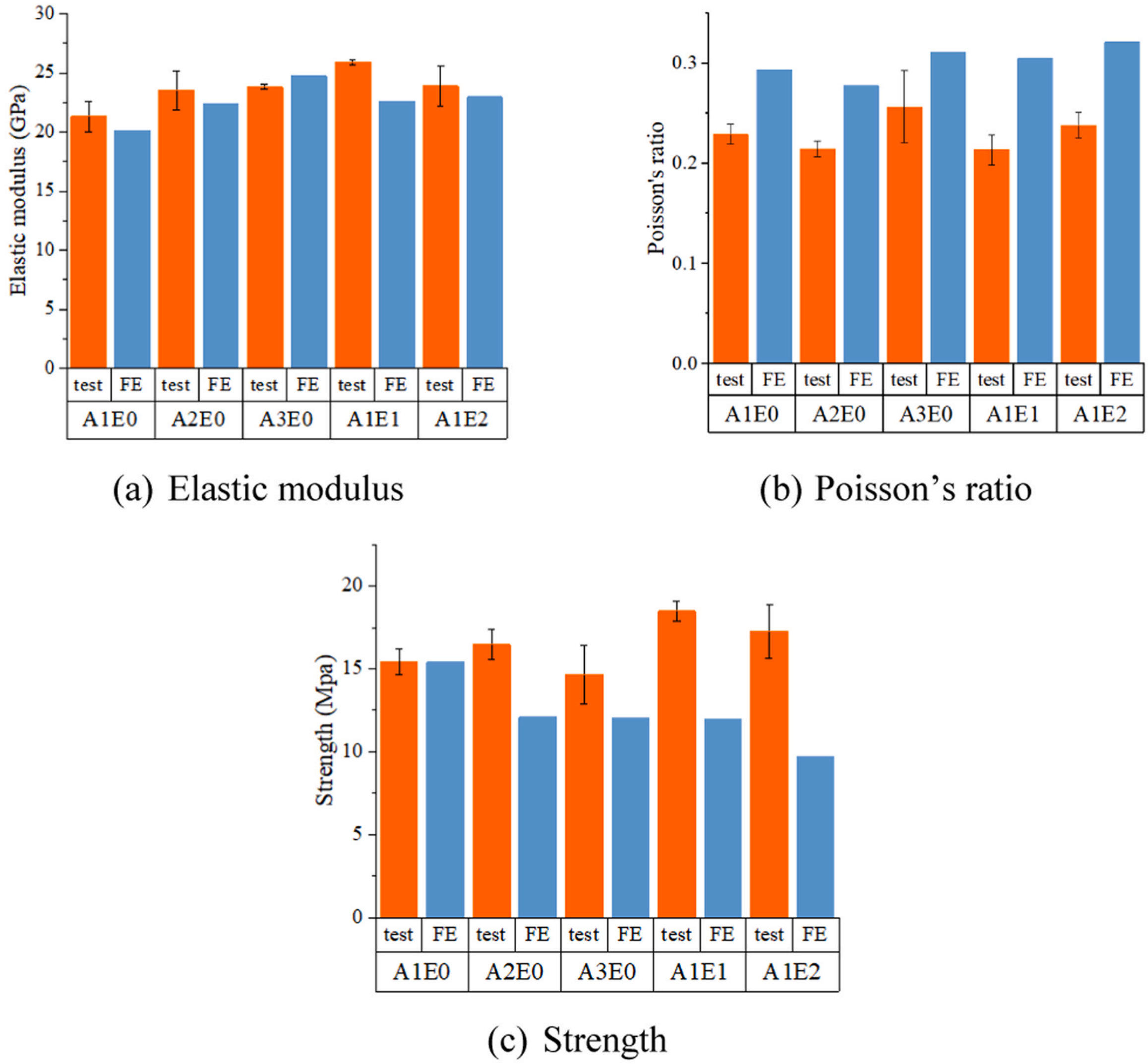

Fig. 15. Mechanical parameters for the test and FE model.

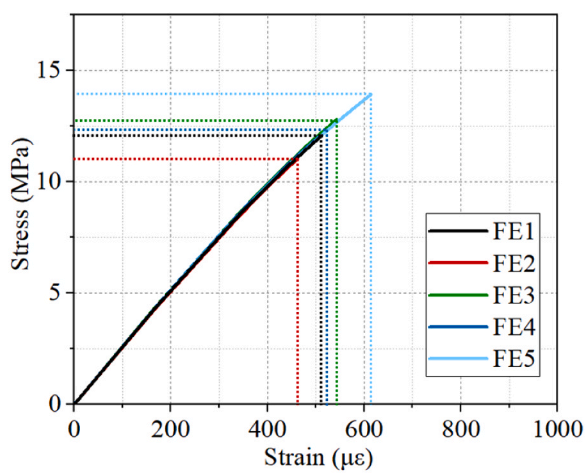

Fig. 16. FE repeatability analysis of A3E0.

4.4. Repeatability analysis

Similar to the test results, randomness existed in the physics engine simulations. A repeatability analysis was conducted on the FE model, the results of which are shown in Fig. 16. For ease of calculation, the analysis was performed based on the A3E0 group, which had the largest aggregate size. FE1 is the A3E0 model analyzed in Section 4.3. The aggregate fractions of all the models were in the range 52.15–54.15 %. The FE model exhibited consistent results in the initial stage. However, after local failure occurred in the model, variations in the ultimate strain and stress were observed. The maximum strength exceeded the minimum strength by 26 %. This inconsistency further verified the inherent randomness of the aggregate skeleton.

4.5. Influence of aggregate shape

To study the influence of flat and elongated aggregate on the PAC properties, FE models with different aggregate shapes were established. During aggregate generation in the physics engine, convex polyhedral points were obtained from ellipsoids rather than from spheres. The lengths of the three axes of ellipsoid are denoted as d_1, d_2, and d_3 ($d_1 \geq d_2 \geq d_3$). The four selected ellipsoidal shapes are listed in Table 6. When sieving the aggregates, the size of the sieve hole corresponded approximately to the minimum cross-sectional area of the aggregates. Therefore, d_3 was equivalent to the sieve size of the aggregates. The stacking state of the aggregates in the formwork is shown in Fig. 17. The aggregate fraction was mainly controlled by d_1. The impact of d_2 on the aggregate fraction was minimal, and its influence was not significant. This suggests that elongated aggregates exert a more pronounced effect on PAC than flat aggregates.

FE models were established based on geometric models. All groups selected the E0 grout without expansive agent added. The stress–strain curves are shown in Fig. 18. The FE models arranged in decreasing order of the elastic modulus are A3e3E0, A3e2E0, A3e4E0, A3e1E0, and A3E0. There was a strong positive correlation between the elastic modulus and single aggregate volume, whereas the correlation with the aggregate fraction was relatively weak. Owing to the poor mechanical properties of the ITZ without expansive agent, the elastic modulus and strength of PAC could be improved by appropriately increasing the volume of a single aggregate.

5. Shrinkage simulation discussion

5.1. Finite element model

The specimen size for the shrinkage behavior test was too large for mesoscale simulation. Therefore, an FE model of the same size as the mechanical properties was chosen to simulate the shrinkage behavior. During the physics engine simulation process, the aggregates were placed vertically. Owing to the different directions of aggregate stacking, the shrinkage and mechanical models of the same aggregate grading had different aggregate fractions. Considering the A1E0 group as an example, the shrinkage FE model is shown in Fig. 19. The grout, ITZ, and aggregates were all considered elastic materials owing to the minimal free shrinkage of PAC. The elastic modulus and Poisson's ratio of the material as well as the boundary conditions and element types were the same as those in Section 4.2. The free-shrinkage process of the grout and ITZ was simulated using a temperature field. Because shrinkage and elastic deformation are both elastic behaviors, the same reduction coefficient as the elastic modulus was used to determine the shrinkage of the ITZ. In other words, the shrinkage of the ITZ was considered to be 1/3 of the grout shrinkage.

5.2. Comparison of test and simulation

5.2.1. Grout shrinkage

The shrinkage measurement results for grouts E0, E1, and E2 are presented in Fig. 20. For consistency with the PAC test, the grout specimens were measured from the third day after casting. For the E0 grout without expansive agent, the relationship between the shrinkage strain and time was approximately linear. After 40 d, the shrinkage strain of the E0 grout reached 452 με.

The addition of the expansive agent significantly reduced the shrinkage strain. In comparison with E1, the shrinkage strain of E2 was smaller and exhibited expansion, indicating a stronger expansion effect of the MgO expansive agent. Furthermore, there were differences in the reaction times of the two expansive agents. The effect of the CSA expansive agent was mild, and the shrinkage strain of the E1 grout stabilized after a rapid increase in the early stages. The influence of MgO persisted for an extended period. The expansion of the E2 specimen continued until 40 d. Meanwhile, the shrinkage strain of specimen E2 exhibited greater fluctuation, reflecting the lower soundness of MgO [30].

Table 6
Shape of ellipsoids in aggregate generation.

ID	d_1: d_2: d_3
A3e1	2: 1: 1
A3e2	2: 2: 1
A3e3	4: 2: 1
A3e4	4: 1: 1

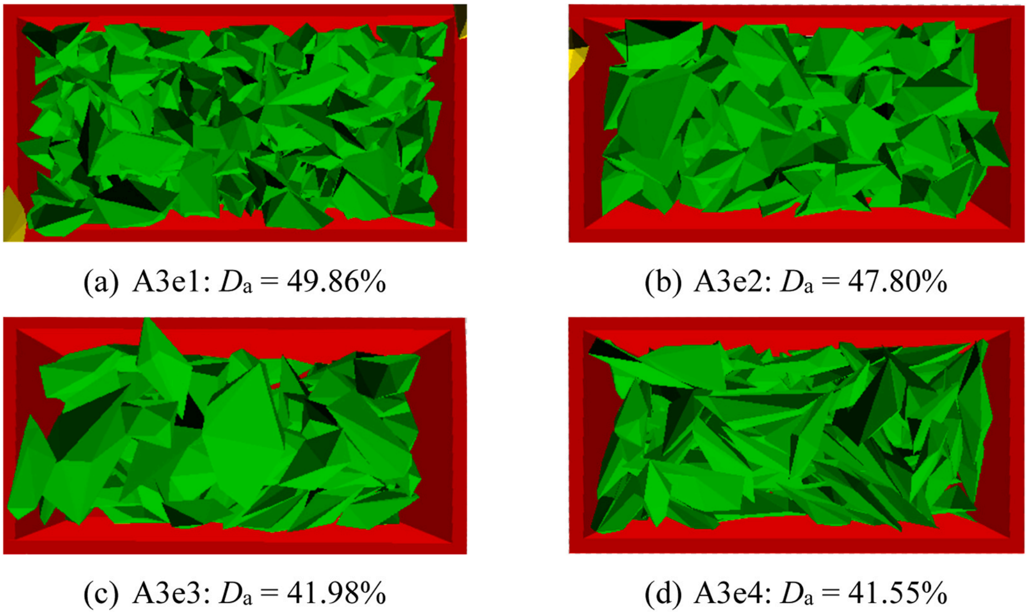

Fig. 17. Stacking state of different aggregate shapes.

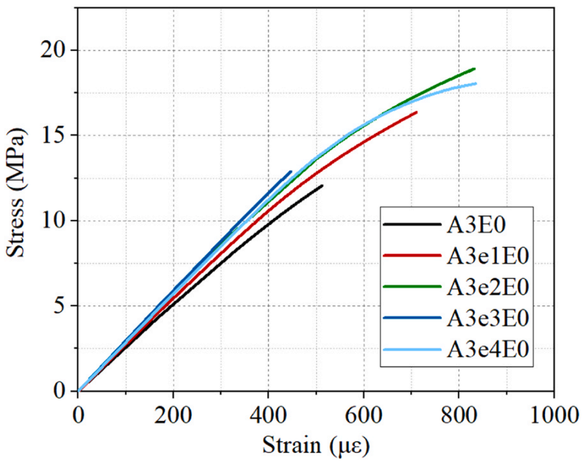

Fig. 18. Stress–strain curve of FE models with different aggregate shapes.

5.2.2. *Shrinkage strain curve*

The grout shrinkage results were input into the FE model. The shrinkage properties of the ITZ were those of the grout multiplied by a reduction factor of 1/3. Taking the A1E0 model as an example, Fig. 21 shows the calculated longitudinal deformation distribution. Owing to the uneven distribution of the grout and aggregates, the deformation was also uneven in the horizontal and longitudinal directions. To avoid this nonuniformity, the middle 202.5 mm was selected as the measurement section. The average value of the midpoints on the four sides was considered as the deformation value, and the strain was obtained from the deformation at both ends of the measurement section.

Fig. 22 illustrates the shrinkage strains of the test specimens and FE models. Owing to the elastic behavior of the FE model, the shrinkage strain in the overall model was proportional to that of the grout input into the model. A difference was observed between the FE and experimental results. This difference indicates that the grout and PAC specimen shrinkage involved distinct mechanisms. The shrinkage of the PAC specimen without an expansive agent followed a two-stage mode:

Stage I: Steady growth stage. This stage occurred approximately during 0–8 d. During this period, the growth rate of the simulated shrinkage strain was lower than that in the test results. This is due to the accumulation of temperature in the mass concrete [43]. Increasing the temperature promoted evaporation and accelerated shrinkage. However, the FE and test results showed a similar pattern of aggregate grading influence on the shrinkage performance. The early-stage shrinkage of A3E0 was greater than that of A1E0 and A2E0, indicating that larger aggregate sizes lead to increased early shrinkage.

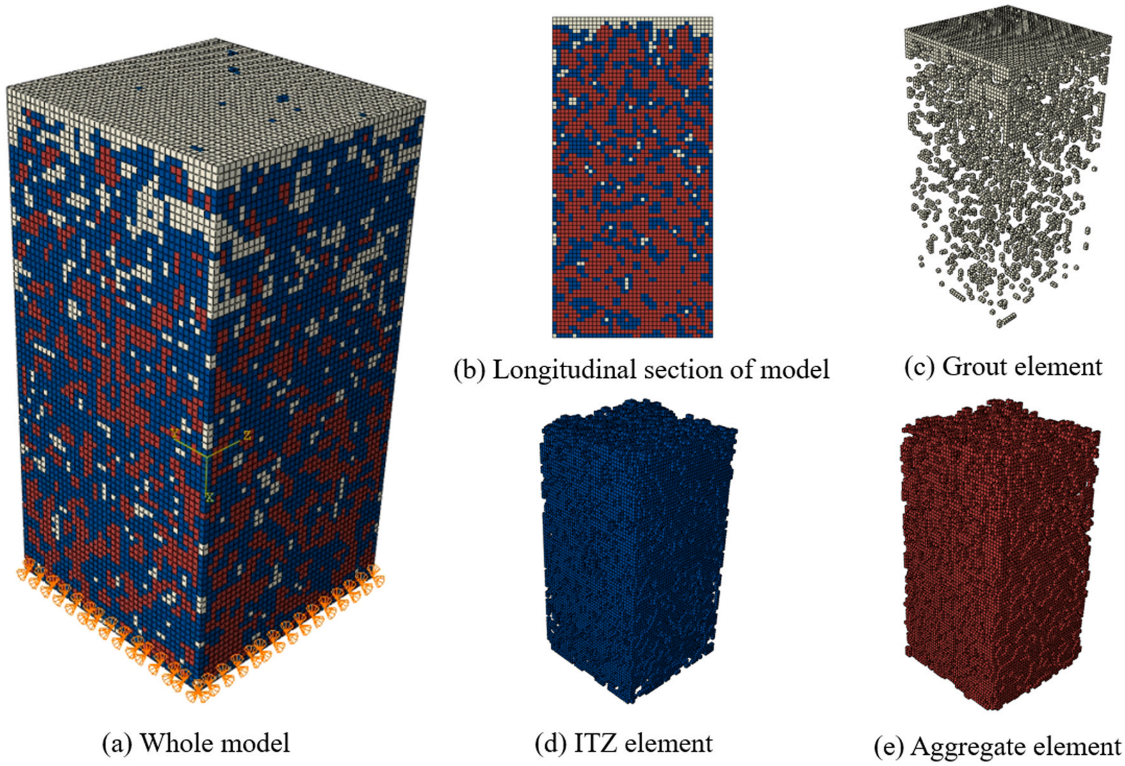

Fig. 19. Shrinkage FE model of the A1E0 specimen.

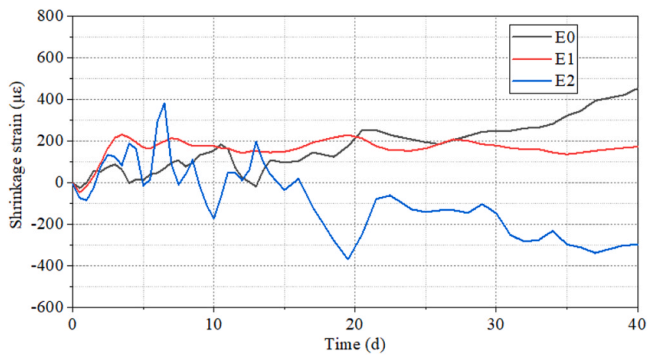

Fig. 20. Shrinkage strain for the E0, E1, and E2 grout.

Stage II: Strain stabilization stage. This stage occurred approximately during 8–40 d. During this period, the change in the shrinkage strain was no longer significant. After the surface moisture evaporated, it was difficult for the internal moisture to evaporate and diffuse because of the large size of the PAC specimens. The internal shrinkage stabilized quickly, and as the surface moisture evaporated, the overall shrinkage stabilized. Small aggregates could form a dense ITZ network, which was conducive to internal moisture diffusion. This led to a lower shrinkage strain in A3E0 compared to A1E0 and A2E0 at this stage.

After the addition of the expansive agent, the shrinkage of PAC was noticeably mitigated and even converted to expansion. The expansive strain caused by the expansive agent was obtained by subtracting the strains of specimens A1E1 and A1E2 from that of the A1E0 specimen, as shown in Fig. 23. Similar to the shrinkage behavior of the grout, the expansion of the A1E2 specimen was higher than that of the A1E1 specimen. In Stage I, the expansion effects of the two expansion agents were superior to those of the simulated results. This may be attributed to the accumulated temperature in PAC, which promoted the reaction of the expansive agent. In Stage II, the accumulated temperature was released, and the expansion rate of the FE models was essentially the same as that of the test models.

The results show that the PAC and grout had different shrinkage conditions. In Stage I, the heat generated from cement hydration was difficult to dissipate, leading to an increase in specimen temperature. This significantly enhanced both the shrinkage strain of grout and the expansion strain induced by the expansive agent. In Stage II, the smaller specific surface area of PAC specimen makes it

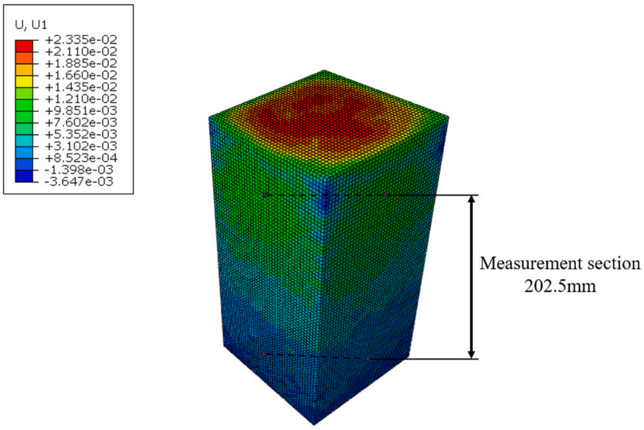

Fig. 21. Longitudinal deformation distribution of the A1E0 model.

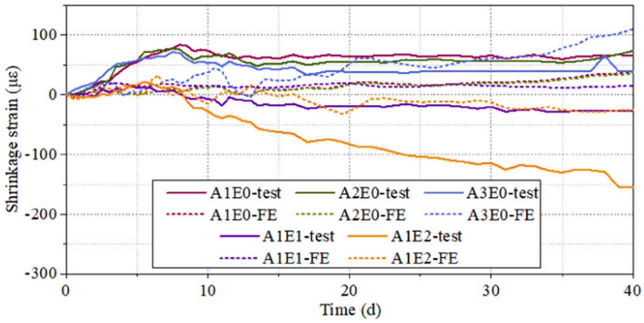

Fig. 22. Shrinkage strain of test specimens and FE models.

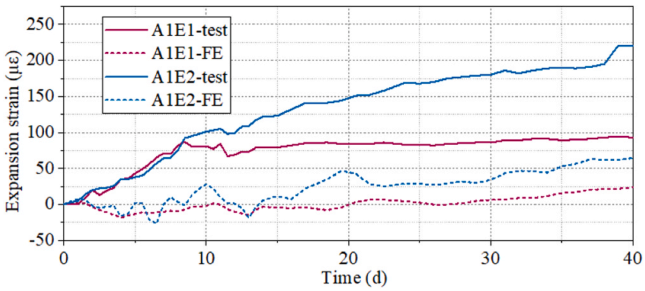

Fig. 23. Expansion strain of test specimens and FE models (only for A1E1 and A1E2).

harder for internal moisture to evaporate, thereby inhibiting shrinkage. Consequently, PAC specimens no longer exhibit continuous shrinkage behavior like grout specimens. At this stage, the expansion strain obtained from the FE model aligned well with experimental results. Therefore, deducing the accurate shrinkage curve of PAC from a single-grout shrinkage curve is challenging. It is essential to establish shrinkage curves for grout tests under different drying and sealing conditions. A more refined FE model can be developed based on the shrinkage conditions and temperature field distribution of the grouts at different locations in the PAC specimens.

5.3. Relationship between aggregate fraction and PAC shrinkage

Although the FE model cannot directly predict the relationship between the PAC shrinkage and grout shrinkage, it can be used to evaluate the relationship when the shrinkage conditions are consistent. By denoting the shrinkage strain of the PAC model as ε_p and the shrinkage strain of grout as ε_g, the shrinkage coefficient α_s can be defined as:

$$\alpha_s = \varepsilon_g / \varepsilon_p \tag{3}$$

Similar to the mechanical property simulation, repeatability and aggregate shape influence analyses of A3E0 were conducted. the aggregate fraction D_a was obtained for each model using the physics engine, and the shrinkage coefficient α_s was calculated for each model by the FE model. Combining the previously calculated shrinkage results of the A1E0, A2E0, and A3E0 models, the relationship between D_a and α_s was obtained, as shown in Fig. 24. The expansive agent had little effect on the grout elastic modulus. It can be considered that under different grout types, the same aggregate grading has the same α_s. The definition of the A3e series was consistent with that described in Section 4.5. α_s increased nonlinearly with an increase in D_a. Satisfying $\alpha_s \to +\infty$ ($D_a = 100$ %) and $\alpha_s = 1$ ($Da = 0$), the fitting curve could be obtained. A3 in the different simulations and different aggregate shapes showed a good fit with the fitting curve.

6. Conclusion

In this study, physics engine was introduced to PAC mesoscale simulation. This novel simulation method addressed the limitations of traditional approaches in accurately simulating the coarse aggregate skeleton. Mechanical property and shrinkage tests were performed on PAC, considering the impact of aggregate size and expansive agents. Test specimens were simulated using this mesoscale simulation method, and the mechanical properties and shrinkage behaviors of the test and simulation were compared. The following conclusions were drawn from this study:

(1) To verify the accuracy of the novel method, the simulated aggregate fraction was compared with the test results. The results showed that the simulated aggregate fraction could reach a high level of 60 % and closely aligned with the test results. The discrepancy could be attributed to the sharp shape effect and the contact coverage. In the FE model, the breakpoints were present in the vertical direction of the aggregate skeleton. This indicates the absence of an integral aggregate skeleton at the 2D level and verifies the necessity of the 3D model. The aggregate shape analysis revealed that the aggregate fraction was primarily influenced by the longest axis of the circumscribed ellipsoid. Elongated aggregates had a more pronounced effect on the aggregate fraction than flat aggregates.

(2) In the mechanical property test, the cracks mostly developed longitudinally and attached to the aggregates. Crack propagation was concentrated near the edges and corners, leading to grout detachment. Because the overall aggregate skeleton could still bear the load after local failure, some specimens exhibited good ductility in the stress–strain curve. The FE model and test specimens exhibited similar variation tendencies in the elastic modulus and Poisson's ratio. However, owing to the limitations of the FE method, simulating the later stage of the concrete spalling process was challenging, which resulted in a lower simulated strength. The aggregate shape influence analysis showed that the elastic modulus of PAC was mainly affected by the volume of the individual aggregates.

(3) The shrinkage of the PAC specimen without expansive agent followed a two-stage mode: Stage I (steady growth stage) and Stage II (strain stabilization stage). Owing to the elastic behavior of the FE model, the shrinkage strain in the overall model was proportional to that of the grout input to the model. Discrepancies existed between the FE and test results, which were attributed to the diverse shrinkage conditions in the curing process, surface area, and interior area. To obtain a more accurate simulation, it is essential to establish shrinkage curves for grout tests under different conditions, such as drying and sealing. The shrinkage coefficient α_s reflecting the relationship between grout and PAC shrinkage was proposed. The relationship between the aggregate fraction and α_s was obtained through a fitting curve, which can be used to assess the impact of different aggregate fractions on PAC shrinkage.

(4) This novel mesoscale simulation method based on a physics engine is particularly suitable for PAC. The simulation yields relatively good results. However, this method is not limited to PAC and can be applied to the simulation of conventional concrete, thus solving the problem of traditional simulation methods that struggle to achieve a high aggregate fraction. However, unlike PAC, gaps exist between the aggregates in traditional concrete. During the aggregates throwing process, these gaps can be considered by expanding the aggregate size.

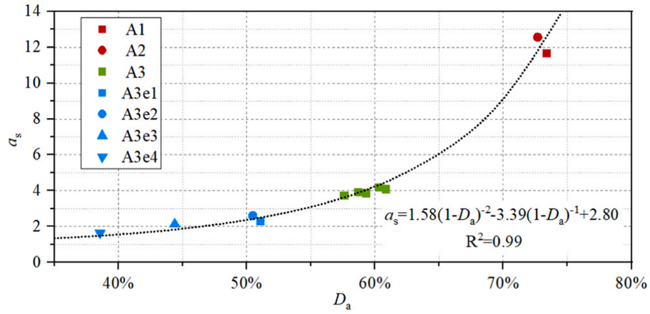

Fig. 24. Relationship between the aggregate fraction and shrinkage coefficient.

CRediT authorship contribution statement

Chongfeng Xie: Writing – original draft, Methodology, Investigation, Conceptualization. **Charun Bao:** Methodology, Investigation. **Xiwang Chen:** Writing – review & editing, Supervision, Conceptualization. **Jia-Qi Yang:** Methodology, Investigation, Conceptualization. **Peng Feng:** Writing – review & editing, Supervision, Funding acquisition.

Declaration of Competing Interest

The authors declare that they have no known competing financial interests or personal relationships that could have appeared to influence the work reported in this paper.

Data availability

Data will be made available on request.

Acknowledgements

This research has been supported by the National Natural Science Foundation of China (No. U2106219), CNPC Offshore Engineering Company Limited (No. 2019B-3203), and the Guoqiang Institute, Tsinghua University (No. 2021GOG1001). The first author Chongfeng Xie was supported by the Program Fund of Non-Metallic Excellence and Innovation Center for Building Materials (No. 2023Ph. D-1).

References

[1] M.F. Najjar, A.M. Soliman, M.L. Nehdi, Critical overview of two-stage concrete: properties and applications, Constr. Build. Mater. 62 (2014) 47–58.
[2] S. Champion, L. Davis, Grouted concrete construction, Reinf. Concrete Rev. (1958) 569–608.
[3] A.S. Abdul Awal, Creep recovery of prepacked aggregate concrete, J. Mater. Civil Eng. 4 (1992) 320–325.
[4] R.J. Vishwakarma, P. Kumari, S.G. Morkhade, P.V. Bahekar, Engineering properties of two-stage concrete: a critical review, Mater. Today Proceedings 77 (2023) 729–733.
[5] J.Y. Yoon, J.H. Kim, Mechanical properties of preplaced lightweight aggregates concrete, Constr. Build. Mater. 216 (2019) 440–449.
[6] H.S. Abdelgader, Effect of the quantity of sand on the compressive strength of two-stage concrete, Magazine Concr. Res. 48 (1996) 353–360.
[7] J. O'Malley, H.S. Abdelgader, Investigation into viability of using two-stage (pre-placed aggregate) concrete in Irish setting, Front. Architecture Civil Eng. China 4 (2010) 127–132.
[8] P.S.M. Thilakarathna, K.K. Baduge, P. Mendis, V. Vimonsatit, H. Lee, Mesoscale modelling of concrete–a review of geometry generation, placing algorithms, constitutive relations and applications, Eng. Fract. Mech. 231 (2020) 106974.
[9] Y. Yu, Y. Zheng, X.-Y. Zhao, Mesoscale modeling of recycled aggregate concrete under uniaxial compression and tension using discrete element method, Constr. Build. Mater. 268 (2021) 121116.
[10] J. Zhou, M. Zheng, Q. Zhan, R. Zhou, Y. Zhang, Y. Wang, Discrete element modelling of the uniaxial compression behavior of pervious concrete, Case Stud. Constr. Mater. 18 (2023) e01937.
[11] Y. Yu, J. Xu, J. Su, L. Xu, Y. Luo, Investigating specimen size and shape effects on compressive mechanical behaviors of recycled aggregate concrete using discrete element mesoscale modeling, Constr. Build. Mater. 438 (2024) 137196.
[12] A. Yin, X. Yang, C. Zhang, G. Zeng, Z. Yang, Three-dimensional heterogeneous fracture simulation of asphalt mixture under uniaxial tension with cohesive crack model, Constr. Build. Mater. 76 (2015) 103–117.
[13] H. Ma, W. Xu, Y. Li, Random aggregate model for mesoscopic structures and mechanical analysis of fully-graded concrete, Comput. Struct. 177 (2016) 103–113.
[14] J. Zhang, Z. Wang, H. Yang, Z. Wang, X. Shu, 3D meso-scale modeling of reinforcement concrete with high volume fraction of randomly distributed aggregates, Constr. Build. Mater. 164 (2018) 350–361.
[15] Y.-j Huang, F.-q Guo, H. Zhang, Z.-j Yang, An efficient computational framework for generating realistic 3D mesoscale concrete models using micro X-ray computed tomography images and dynamic physics engine, Cem. Concr. Compos. 126 (2022).
[16] H.-K. Man, J. Van Mier, Damage distribution and size effect in numerical concrete from lattice analyses, Cem. Concr. Compos. 33 (2011) 867–880.
[17] Z. Tan, F.-q Guo, Z. Leng, Z.-j Yang, P. Cao, A novel strategy for generating mesoscale asphalt concrete model with controllable aggregate morphology and packing structure, Comput. Struct. 296 (2024) 107315.
[18] S. Longshaw, M. Turner, E. Flinch, R. GawthorpeAnalyzing the use of real-time physics engines for scientific simulation: exploring the theoretical and practical benefits for discrete element modeling Proceedings of the 18th Conference on Computational Mechanics (ACME-UK) , 2010.
[19] Z. Zheng, C. Zeng, X. Wei, J. Chen, Parameterized implementation of a triple refined modeling framework for mesoscale concrete, Constr. Build. Mater. 346 (2022).
[20] H. Ouyang, X. Chen, 3D meso-scale modeling of concrete with a local background grid method, Constr. Build. Mater. 257 (2020).
[21] G. Li, Y. Zhao, S.-S. Pang, Four-phase sphere modeling of effective bulk modulus of concrete, Cem. Concr. Res. 29 (1999) 839–845.
[22] Qu, J., Cherkaoui, M., Fundamentals of micromechanics of solids, Wiley Online Library2006.
[23] H.S. Abdelgader, J. Górski, Stress-strain relations and modulus of elasticity of two-stage concrete, J. Mater. Civil Eng. 15 (2003) 329–334.
[24] P.R. Stodola, D. Akers, J. Bennet Jr, A. Cheff, T. Clapp, J. Cope, D. Green, Guide for the use of preplaced aggregate concrete for structural and mass concrete applications, ACI Mater. J. 88 (1992) 650–668.
[25] M. Coo, T. Pheeraphan, Effect of sand, fly ash and limestone powder on preplaced aggregate concrete mechanical properties and reinforced beam shear capacity, Constr. Build. Mater. 120 (2016) 581–592.
[26] M. Tuyan, L.V. Zhang, M.L. Nehdi, Development of sustainable preplaced aggregate concrete with alkali-activated slag grout, Constr. Build. Mater. 263 (2020).
[27] H.S. Abdelgader, M. Kurpińska, M. Amran, Effect of slag coal ash and foamed glass on the mechanical properties of two-stage concrete, Mater. Today Proceed. 58 (2022) 1091–1097.
[28] K.K. Das, E.S.-S. Lam, J.G. Jang, Effects of modified binders on flowability of grout and properties of preplaced aggregate concrete, J. Build. Eng. 68 (2023).
[29] G. Ou, T. Kishi, L. Mo, Z. Lin, New insights into restrained stress and deformation mechanisms of concretes blended with calcium sulfoaluminate and MgO expansive additives using multi-scale techniques, Constr. Build. Mater. 371 (2023).
[30] L. Mo, M. Deng, M. Tang, A. Al-Tabbaa, MgO expansive cement and concrete in China: past, present and future, Cement and concrete research 57 (2014) 1–12.
[31] GB/T 29756–2013, Test methods of physical property for dry-mix mortar, Beijing, China: China Standardization Administration, 2013. (in Chinese).

[32] GB/T 50081–2019, Standard for test methods of concrete physical and mechanical properties, Beijing, China: China Architecture & Building Press, 2019. (in Chinese).
[33] JGJ/T 70–2009, Standard for test method of basic properties of construction motar, Beijing, China: China Industry Press, 2009. (in Chinese).
[34] L. Jin, W. Yu, X. Du, S. Zhang, D. Li, Meso-scale modelling of the size effect on dynamic compressive failure of concrete under different strain rates, Int. J. Impact Eng. 125 (2019) 1–12.
[35] H. Chen, B. Xu, J. Wang, T. Zhou, X. Nie, Y.L. Mo, Parametric analysis on compressive strain rate effect of concrete using mesoscale modeling approach, Constr. Build. Mat. 246 (2020) 118375.
[36] X. Hu, C. Shi, Z. Shi, L. Zhang, Compressive strength, pore structure and chloride transport properties of alkali-activated slag/fly ash mortars, Cem. Concr. Compos. 104 (2019) 103392.
[37] J. Lubliner, J. Oliver, S. Oller, E. Oñate, A plastic-damage model for concrete, Int. J. Solids Struct. 25 (1989) 299–326.
[38] W. Yuan, Y. Xiaojing, W. Kai, H. Tianhai, Expermental study on the stress-strain curve of cementitious grout under uniaxial compression, Ind. Constr. 44 (2014) 909–913. +903. (in Chinese).
[39] Z. Zhu, H. Chen, Overestimation of ITZ thickness around regular polygon and ellipse aggregate, Comput. Struct. 182 (2017) 205–218.
[40] M. Maleki, I. Rasoolan, A. Khajehdezfuly, A.P. Jivkov, On the effect of ITZ thickness in meso-scale models of concrete, Constr. Build. Mat. 258 (2020) 119639.
[41] L. Jin, S. Wan, D. Li, L. Miao, X. Du, Influence of concrete strength and aggregate size on the size effect of shear capacity of RC beam-column joints under monotonic loading: Mesoscale numerical tests, Structures 37 (2022) 671–685.
[42] S.-M. Kim, R.K. Abu Al-Rub, Meso-scale computational modeling of the plastic-damage response of cementitious composites, Cem. Concr. Res. 41 (2011) 339–358.
[43] Y. Hu, J. Chen, F. Zou, M. He, J. Mao, X. Liu, C. Zhou, Z. Yuan, A comparative study of temperature of mass concrete placed in August and November based on on-site measurement, Case Stud. Constr. Mater. 15 (2021) e00694.